SF2A 2016
C. Reylé, J. Richard, L. Cambrésy, M. Deleuil, E. Pécontal, L. Tresse and I. Vauglin (eds)

MULTIWAVELENGTH STUDY OF THE FLARING ACTIVITY OF SGR A* IN 2014 FEBRUARY–APRIL

E. Mossoux[1], N. Grosso[1], H. Bushouse[2], A. Eckart[3, 4], F. Yusef-Zadeh[5], R. L. Plambeck[6], F. Peissker[3], M. Valencia[3], D. Porquet[1], W. D. Cotton[7] and D. A. Roberts[5]

Abstract. The supermassive black hole Sgr A* is located at the Milky Way center. We studied its flaring activity close to the DSO/G2 pericenter passage with XMM-Newton, HST/WFC3, VLT/SINFONI, CARMA and VLA to constrain the physical properties and origin of the flares. We detected two X-ray and three NIR flares on 2014 Mar. 10 and Apr. 2 with XMM-Newton and HST and two NIR flares on 2014 Apr. 3 and 4 with VLT. The 2014 Mar. 10 X-ray flare has a long rise and a rapid decay. Its NIR counterpart peaked 4320 s before the X-ray peak implying a variation in the X-ray-to-NIR flux ratio. This flare may be a single flare where change in the flux ratio is explained by the adiabatic compression of a plasmon or two close flares with simultaneous X-ray/NIR peaks. We observed an increase in the rising radio flux density on 2014 Mar. 10 with the VLA. It could be the delayed emission from a NIR/X-ray flare preceding our observation. The 2014 Apr. 2 X-ray flare occurred for HST in the Earth occultation of Sgr A*. We thus only observed the start of its NIR counterpart. After the occultation, we observed the decay phase of a bright NIR flare with no X-ray counterpart. On 2014 Apr. 3, two CARMA flares were observed. The first one may be the delayed emission of a VLT NIR flare. We thus observed a total of seven NIR flares whose three have an X-ray counterpart. We studied the physical parameters of the flaring region for each NIR flare but none of the possible radiative processes can be ruled out for the X-ray flares creation. Our X-ray flaring rate is consistent with those observed in the 2012 Chandra XVP campaign. No increase in the flaring activity was thus triggered close to the DSO/G2 pericenter passage. Moreover, higher X-ray flaring rates had already been observed with no increase in the quiescent level. There is thus no direct link between an X-ray flaring-rate increase and an accretion-rate change.

Keywords: Galaxy: center, X-rays: Sgr A*, radiation mechanisms: general

1 Introduction

Our Galaxy hosts Sgr A* the closest supermassive black hole at a distance of about 8 kpc (Genzel et al. 2010; Falcke & Markoff 2013). It has a mass $M_{\rm BH} = 4 \times 10^6\ M_\odot$ (Schödel et al. 2002; Ghez et al. 2008; Gillessen et al. 2009) and is usually in a non-flaring state, emitting predominately in radio to submillimeter wavelengths. Above this steady level, flares in near-infrared (NIR), X-rays and radio are observed. The NIR emission from Sgr A* is an overall flaring activity mostly with low amplitude, with several brighter flares up to 32 mJy (Witzel et al. 2012). The X-ray emission is composed by a non-flaring state plus a flaring activity characterized by a flaring rate of 1.1 $(1.0 - 1.3)$ flare per day with an intrinsic flare luminosity larger than 10^{34} erg s^{-1} in the 2–8 keV energy band (Neilsen et al. 2013). When NIR and X-ray flares are detected simultaneously, their light curves have similar shapes with a delay shorter than 3 min between their maximum (e.g., Yusef-Zadeh et al. 2006; Dodds-Eden et al. 2009; Eckart et al. 2012). While NIR flares are known to be due to synchrotron emission

---

[1] Observatoire Astronomique de Strasbourg, Université de Strasbourg, CNRS, UMR 7550, 11 rue de l'Université, F-67000 Strasbourg, France.

[2] Nicolaus Copernicus Astronomical Center, ul. Bartycka 18, 00-716 Warszawa, Poland.

[3] Physikalisches Institut der Universität zu Köln, Zülpicher Str. 77, 50937 Köln, Germany

[4] Max-Planck-Institut für Radioastronomie, Auf dem Hügel 69, 53121 Bonn, Germany.

[5] Department of Physics and Astronomy, CIERA, Northwestern University, Evanston, IL 60208, USA.

[6] Radio Astronomy Laboratory, University of California, Berkeley, CA 94720, USA.

[7] National Radio Astronomy Observatory, Charlottesville, VA 22903, USA.

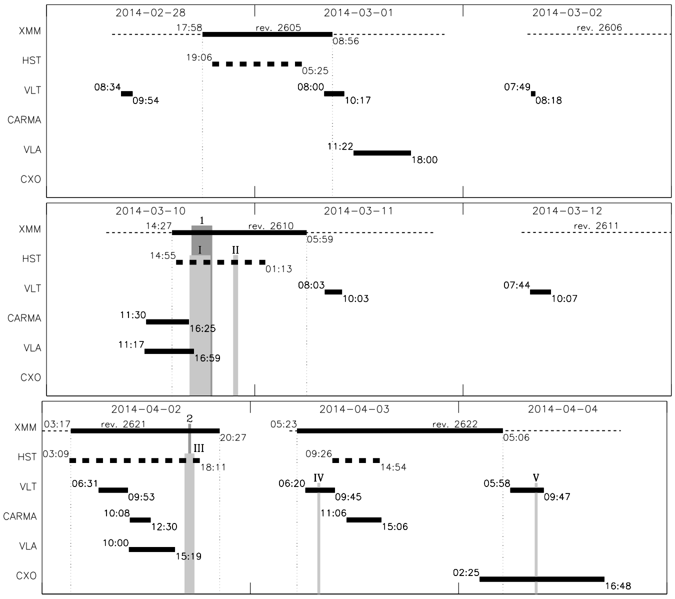

Fig. 1: Time diagram of the 2014 Feb.–Apr. multiwavelength campaign. The horizontal dashed lines are the XMM-Newton orbital visibility times of Sgr A* labeled with revolution numbers. The thick solid lines are the time slot of the observations for each instrument with start and stop hours. The vertical dotted lines are the limits of the XMM-Newton observations. The vertical gray blocks are the detected X-ray (Arabic numerals) and NIR (Roman numerals) flares.

(Eisenhauer et al. 2005; Eckart et al. 2006), the X-ray flare radiative process is still debated with arguments for synchrotron (SYN; Dodds-Eden et al. 2009; Barrière et al. 2014), inverse Compton (IC; Yusef-Zadeh et al. 2012), and synchrotron self-Compton (SSC; Eckart et al. 2008) models. The millimeter and radio flares are delayed by some minutes to hours after the NIR/X-ray flares (Marrone et al. 2008; Yusef-Zadeh et al. 2008, 2009). This behavior is well explained by the adiabatically expanding plasmon model (Van der Laan 1966; Yusef-Zadeh et al. 2006).

On 2011, the G2 object was discovered on its Keplerian orbit toward Sgr A* with a pericenter passage first predicted in mid-2013 (Gillessen et al. 2012). Two hypothesis have been developed on its nature: the first one is that G2 is a compact and ionized cloud of gas (Gillessen et al. 2012, 2013a,b) which would be disrupted during the pericenter passage leading to a putative change of the flare characteristics. The second one is that the G2 is a star with circumstellar matter leading to the name of Dusty S-cluster object (DSO; Eckart et al. 2013; Witzel et al. 2014). In the latter scenario, only a small part of the circumstellar matter would be accreted onto Sgr A*. The best constraints on the DSO/G2 characteristics were reported by Valencia-S. et al. (2015): the DSO/G2 is a pre-main sequence star of $1-2\,M_{\odot}$ with a circumstellar accretion disk emitting a Brγ line thanks to the magnetospheric accretion of circumstellar matter on the stellar photosphere. Its pericenter passage was constrained to 2014 Apr. 20 (Mar. 1– Jun. 10) at $2032\,R_{\rm s}$ corresponding to 163 au from Sgr A* (with $R_{\rm s}=1.2\times10^{12}\,{\rm cm}=0.08\,{\rm au}$ the Sgr A* Schwarzschild radius). These NIR observations made after the pericenter passage proved that DSO/G2 was not tidally disrupted which rejects the purely gas cloud model.

We report here the results published in Mossoux et al. (2016) about the 2014 Feb.–Apr. multiwavelength observations for the study of the effect of the DSO/G2 pericenter passage on the flare activity from Sgr A*.

2 The 2014 Feb.–Apr. multiwavelength observations and flares detection

The 2014 Feb.–Apr. campaign is composed by joint XMM-Newton/HST/VLT observations (XMM-Newton AO-12; PI: N. Grosso) with coordinated/simultaneous observations with HST/WFC3 (F153M filter), VLT/SINFONI (H+K filter), VLA and CARMA (PI: H. Bushouse; A. Eckart; F. Yusef-Zadeh; R. L. Plambeck). The time diagram and the detected X-ray and NIR flares are represented in Fig. 1.

Two X-ray flares (1–2) were automatically detected using the two-steps Bayesian blocks algorithm (Mossoux et al. 2015) with a false positive rate for the flare detection of 0.1%: one on 2014 Mar. 10 and one on Apr. 2. Five NIR flares (I–V) were detected with a 3σ detection limit on the aperture- and extinction-corrected flux density light-curve: two on 2014 Mar. 10, one on Apr. 2, one on Apr. 2 and one on Apr. 3. The start of a possible radio (13.37 GHz = 2.2 cm) was also observed with VLA on 2014 Mar. 10. Three small millimeter flares

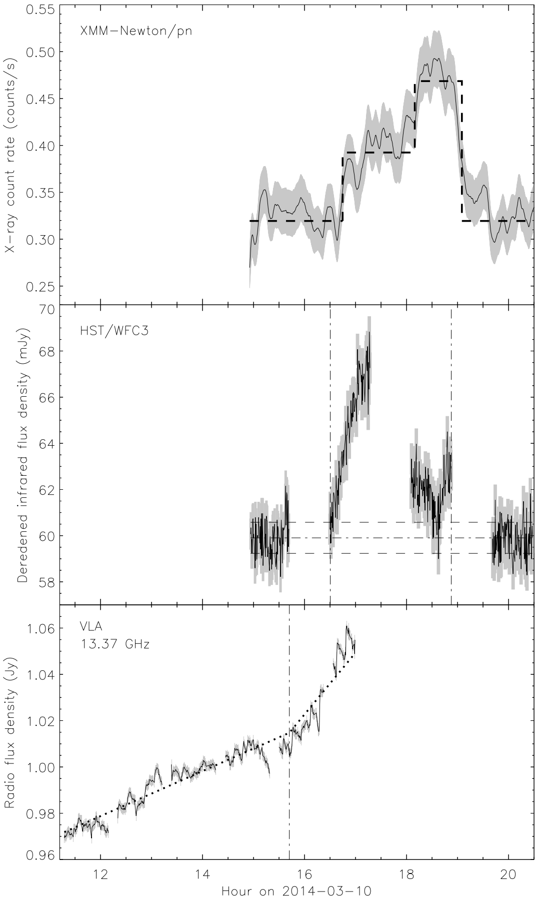

Fig. 2: Simultaneous X-ray, NIR and radio observations of flare I/1 from Sgr A* of 2014 Mar. 10. *Top panel:* The XMM-Newton/EPIC pn smoothed light curve computed with a window width of 500 s and its error in gray. The dashed lines are the Bayesian blocks. *Middle panel:* The deredened HST/WFC3 light curve and its error in gray. The vertical dot-dashed lines are the beginning and the end of the flare. *Bottom panel:* The VLA light curve at 13.37 GHz. The vertical dot-dashed line is the time of the beginning of the flare. The dashed line is the broken slope fit.

(95 GHz = 3.2 mm) were also observed with CARMA: one on 2014 Apr. 2 and two on Apr. 3.

The VLA radio flare of 2014 March 10 begins about 50 min before the NIR/X-ray flare I/1 (Fig. 2) implying that this radio flare is the delayed counterpart of a NIR/X-ray flare occurring before the beginning of the HST and XMM-Newton observations.

The NIR/X-ray flare I/1 is an atypical flare. Indeed, the X-ray light curve is highly asymmetric and characterized by a long rise (7700 s) and a rapid decay (844 s). Moreover, the maximum of the X-ray flare is delayed by $25.5 - 73.9$ min from those of the NIR flare (see Fig. 2). We proposed two interpretations to explain this atypical shape. The first one is the adiabatic compression of a plasmon where the NIR photons are produced by synchrotron radiation and the X-ray photons are due to the SSC process. If the plasmon is compressed, its density increases leading to a more efficient SSC mechanism and thus a lower number of NIR photons reaching the observer. The second interpretation is that the flare I/1 is actually composed by two close subflares (Ia/1a and Ib/1b) produced by their own electron population.

We only observed the decay phase of the NIR flare III on 2014 April 2 just after the occultation of Sgr A* by the Earth (see bottom left panel of Fig. 3). At the end of the previous HST orbit, the flux density from Sgr A* increased slowly.

The first radio flare observed with CARMA on April 3 could be the delayed millimeter counterpart of the NIR flare IV observed with the VLT/SINFONI with a delay of 4.4 h.

3 Constraining the physical parameters of the flaring region

To constrain the physical parameters of the flaring regions, we first determined the NIR–to–X-ray amplitude ratio of the flares detected in NIR and X-rays using a Gaussian fit of the NIR and X-ray light curves (see Fig. 3). Two close Gaussian flares (IIIa and IIIb) are needed to reproduce the light curve of the NIR flare III. The NIR flare IIIa is the simultaneous counterpart of the X-ray flare 2 whereas the NIR flare IIIb has no detected X-ray counterpart.

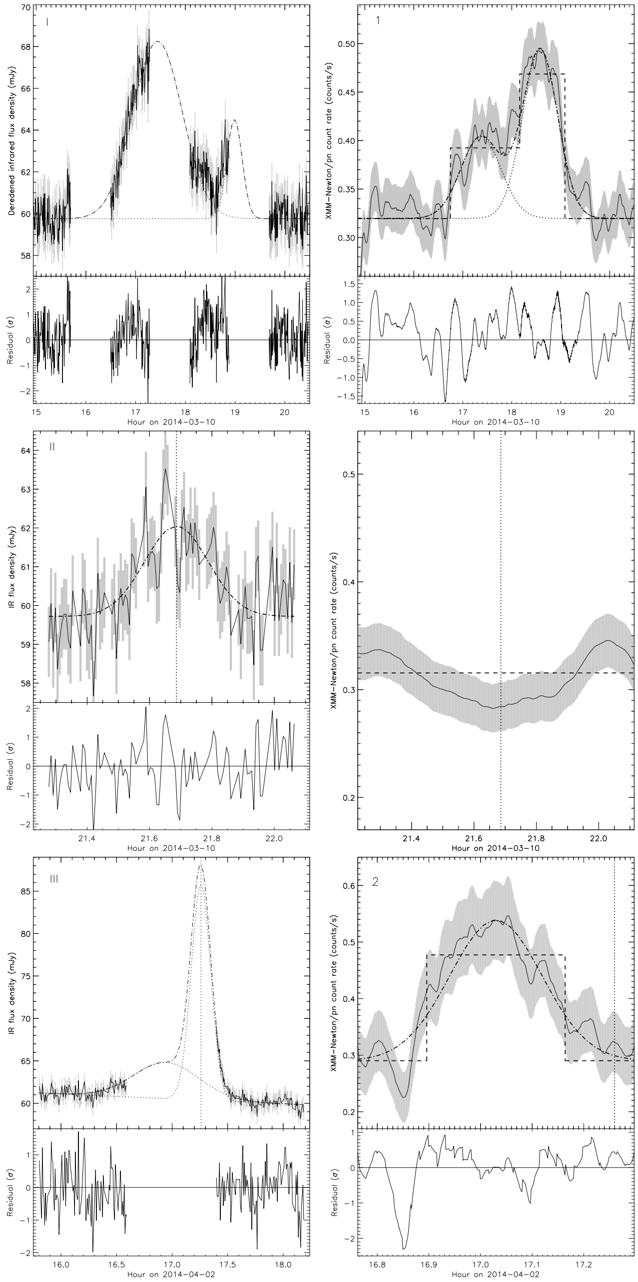

Fig. 3: Gaussian light curve fitting of the HST NIR flares (left panels) and the X-ray counterparts (right panels). The solid lines are the observed light curves with the error bars in gray. The dashed lines in the right panels are the Bayesian blocks. The X-ray light curves are smoothed with an Epanechnikov kernel (parabola shape) with a window width of 500 s and 100 s for 2014 Mar. 10 and Apr. 2, respectively. The dotted lines are the individual Gaussians and the dot-dashed line is the sum of the Gaussians. The vertical dotted lines are the time of the NIR flare peak when there is no detected X-ray counterpart. The residuals are in units of σ.

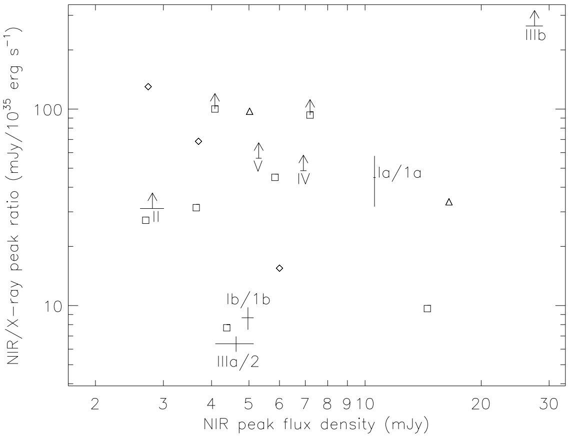

Fig. 4: NIR-to-X-ray peak ratio vs. amplitude of the NIR flares. Squares refer to the flares reported in Table 3 of Eckart et al. (2012). Triangles are the simultaneous NIR/X-ray flares detected on 2007 Apr. 4 and labeled *D* and *E* in Table 2 of Trap et al. (2011). Diamonds are the delayed flares of 2004 Jul. 7, 2008 Jul. 26+27 and 2008 May 5 reported in Table 2 of Yusef-Zadeh et al. (2012). The labeled points are the NIR and X-ray flares observed during this campaign.

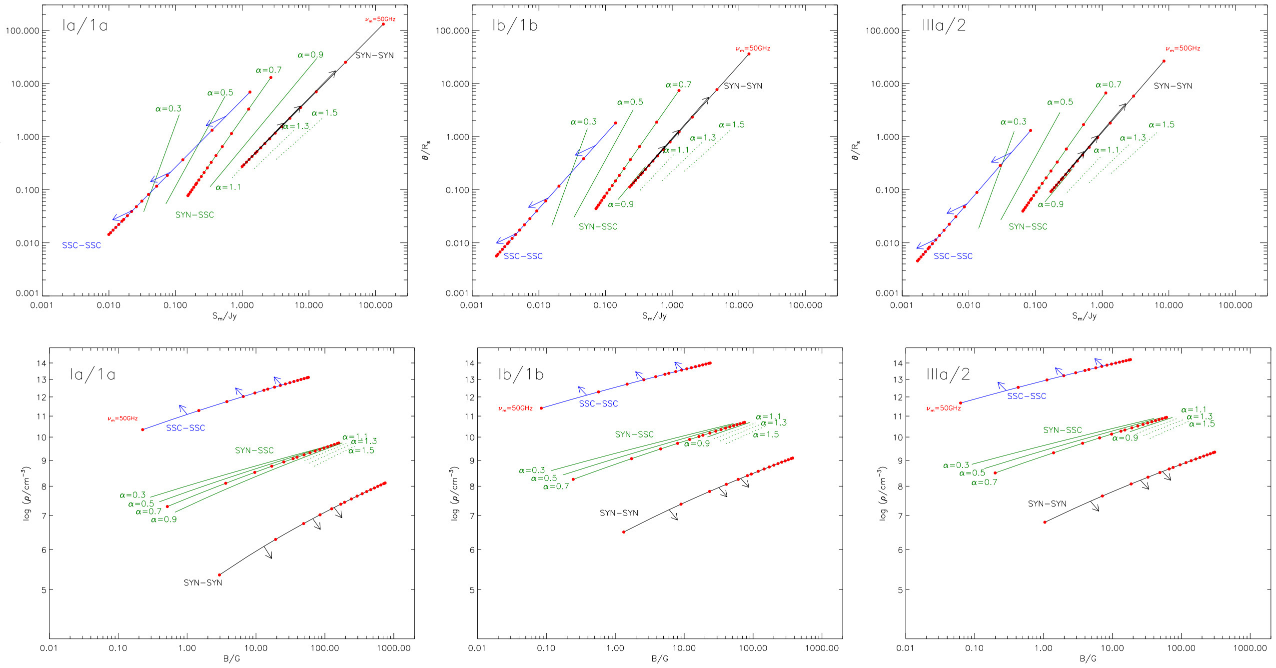

Fig. 5: Physical parameters of the flares observed simultaneously in X-rays and NIR for the three emission models. The flare Ia/1a, Ib/1b and IIIa/2 are in the upper, middle and bottom panels, respectively. Left panels are the size of the flaring-source region (θ) vs. the peak of the spectrum (S_m) at the frequency ν_m. Right panels are the density of the relativistic electrons vs. the magnetic field. The locii where the Synchrotron Self-Compton−Synchrotron Self-Compton (SSC-SSC), Synchrotron−Synchrotron Self-Compton (SYN-SSC) and Synchrotron-Synchrotron (SYN-SYN) are dominant are shown in black, blue and green, respectively. The red dots represent the turnover frequencies from 50 to 3000 GHz by step of 200 GHz. The arrows show the direction of the curves if the limit on the alternative emission processes is lowered. Dotted lines are locii of SYN-SSC where the MIR emission is larger than the observed upper-limit value of 57 mJy at 11.88 μm (Dodds-Eden et al. 2009).

For the NIR flares without detected X-ray counterpart (flares II, IIIb, IV and V), we determined an upper limit with a 95% confidence level on the undetected X-ray amplitude using a Bayesian method (Kraft et al. 1991). The NIR–to–X-ray flux ratio vs. resulting NIR amplitudes are represented among the previously observed NIR/X-ray flares in Fig. 4. The NIR flares with a detected X-ray counterpart are in the bulk of the NIR amplitudes and amplitude ratios already observed. The NIR flare IIIb without detected X-ray counterpart has the largest NIR amplitude and the highest NIR–to–X-ray flux ratio ever observed for a NIR/X-ray flare.

We then used the formalism developed by Eckart et al. (2012) to constrain the physical parameters of the flaring region considering the local radiative processes for the NIR and X-rays: SYN-SYN, SSC-SSC, and SYN-SSC. This formalism is described by six parameters. Two of them are fixed: the turnover frequency (ν_m) and the synchrotron spectral index (α). The four remaining parameters (the size of the source region θ, the magnetic field B, the electron density ρ, and the maximum of the flux density spectrum S_m) are fitted to reproduce the NIR–to–X-ray flux ratio for a given ν_m and α and for a given radiative process. The resulting graphs are shown in Fig. 5. The SYN-SYN, SSC-SSC and SYN-SSC radiative processes are the black, blue and green lines. For the SYN-SYN, SSC-SSC mechanisms, α is given by the amplitude ratio between the NIR and the X-ray flares since there spectrum are supposed to be described by the same spectral index. For the SYN-SSC mechanism, the spectral indexes in NIR and X-rays are not necessarily the same since they are produced by different electron populations. We thus computed the physical parameters for seven values of α from 0.3 to 1.5. We see that the larger the X-ray–to–NIR flare amplitude ratio, the better the physical parameters of the flaring region are constrained. For the NIR/X-ray flare IIIa/2 and the SYN/SSC mechanism, the most constrained parameters are $\theta = 0.03 - 7\,R_\mathrm{s}$ and $\rho = 10^{8.5} - 10^{10.2}\,\mathrm{cm}^{-3}$.

4 Conclusions

We detected 12 flares during the 2014 Feb.–Apr. campaign: seven NIR flares with HST/WFC3 and VLT/SINFONI, three X-ray flares (simultaneous with the three HST flares) with XMM-Newton, one centimeter flare with VLA whose the NIR/X-ray counterpart was not observable and three small millimeter flares with CARMA whose one could be the delayed radio flare of the first NIR flare observed with VLT/SINFONI. Thanks to the NIR–to–X-ray amplitude ratio, we constrained the physical parameters of the flaring regions using the formalism of Eckart et al. (2012). The larger the X-ray–to–NIR flare amplitude ratio, the better the constraints on the physical parameters of the flaring region.

The X-ray flaring rate observed during this campaign (three flares over 255.6 ks) is statistically consistent with those observed during the 2012 *Chandra XVP* campaign using the Bayesian blocks algorithm for the flare detection (1.5 flare per day) implying that no change of the X-ray flaring rate was observed close to the DSO/G2 pericenter passage. The NIR flaring activity observed during the 2014 Feb.–Apr. campaign is also consistent with those previously observed by Witzel et al. (2012) considering the higher detection threshold of the HST/WFC3 and VLT/SINFONI compared to VLT/NACO.

The typical timescale for the accretion of fresh matter from the DSO/G2 object onto Sgr A* at the pericenter is about three years. This timescale is even larger if we consider the large angular momentum of the matter from the DSO/G2 due to its eccentric orbit. We thus would not see any change in the flare characteristics from Sgr A* before 2017.

References

Barrière, N. M., Tomsick, J. A., Baganoff, F. K., et al. 2014, ApJ, 786, 46

Dodds-Eden, K., Porquet, D., Trap, G., et al. 2009, ApJ, 698, 676

Eckart, A., Baganoff, F. K., Schödel, R., et al. 2006, A&A, 450, 535

Eckart, A., García-Marín, M., Vogel, S. N., et al. 2012, A&A, 537, A52

Eckart, A., Mužić, K., Yazici, S., et al. 2013, A&A, 551, A18

Eckart, A., Schödel, R., García-Marín, M., et al. 2008, A&A, 492, 337

Eisenhauer, F., Genzel, R., Alexander, T., et al. 2005, ApJ, 628, 246

Falcke, H. & Markoff, S. B. 2013, Classical and Quantum Gravity, 30, 244003

Genzel, R., Eisenhauer, F., & Gillessen, S. 2010, Reviews of Modern Physics, 82, 3121

Ghez, A. M., Salim, S., Weinberg, N. N., et al. 2008, ApJ, 689, 1044

Gillessen, S., Eisenhauer, F., Fritz, T. K., et al. 2009, ApJ, 707, L114

Gillessen, S., Genzel, R., Fritz, T. K., et al. 2013a, ApJ, 763, 78

Gillessen, S., Genzel, R., Fritz, T. K., et al. 2013b, ApJ, 774, 44

Gillessen, S., Genzel, R., Fritz, T. K., et al. 2012, Nature, 481, 51

Kraft, R. P., Burrows, D. N., & Nousek, J. A. 1991, ApJ, 374, 344

Marrone, D. P., Baganoff, F. K., Morris, M. R., et al. 2008, ApJ, 682, 373

Mossoux, E., Grosso, N., Bushouse, H., et al. 2016, A&A, 589, A116

Mossoux, E., Grosso, N., Vincent, F. H., & Porquet, D. 2015, A&A, 573, A46

Neilsen, J., Nowak, M. A., Gammie, C., et al. 2013, ApJ, 774, 42

Schödel, R., Ott, T., Genzel, R., et al. 2002, Nature, 419, 694

Trap, G., Goldwurm, A., Dodds-Eden, K., et al. 2011, A&A, 528, A140

Valencia-S., M., Eckart, A., Zajaček, M., et al. 2015, ApJ, 800, 125

Van der Laan, H. 1966, Nature, 211, 1131

Witzel, G., Eckart, A., Bremer, M., et al. 2012, ApJS, 203, 18

Witzel, G., Ghez, A. M., Morris, M. R., et al. 2014, ApJ, 796, L8

Yusef-Zadeh, F., Bushouse, H., Wardle, M., et al. 2009, ApJ, 706, 348

Yusef-Zadeh, F., Roberts, D., Wardle, M., Heinke, C. O., & Bower, G. C. 2006, ApJ, 650, 189

Yusef-Zadeh, F., Wardle, M., Dodds-Eden, K., et al. 2012, AJ, 144, 1

Yusef-Zadeh, F., Wardle, M., Heinke, C., et al. 2008, ApJ, 682, 361